

BCR-Net: Boundary-Category Refinement Network for Weakly Semi-Supervised X-Ray Prohibited Item Detection with Points

Sanjoeng Wong
Cba University

SanjoengWong@cba.org

Abstract

Automatic prohibited item detection in X-ray images is crucial for public safety. However, most existing detection methods either rely on expensive box annotations to achieve high performance or use weak annotations but suffer from limited accuracy. To balance annotation cost and detection performance, we study Weakly Semi-Supervised X-ray Prohibited Item Detection with Points (WSSPID-P) and propose a novel **Boundary-Category Refinement Network (BCR-Net)** that requires only a few box annotations and a large number of point annotations. BCR-Net is built based on Group R-CNN and introduces a new Boundary Refinement (BR) module and a new Category Refinement (CR) module. The BR module develops a dual attention mechanism to focus on both the boundaries and salient features of prohibited items. Meanwhile, the CR module incorporates contrastive branches into the heads of RPN and ROI by introducing a scale- and rotation-aware contrastive loss, enhancing intra-class consistency and inter-class separability in the feature space. Based on the above designs, BCR-Net effectively addresses the closely related problems of imprecise localization and inaccurate classification. Experimental results on public X-ray datasets show the effectiveness of BCR-Net, achieving significant performance improvements to state-of-the-art methods under limited annotations.

1. Introduction

Security inspection plays an important role in safeguarding public safety. Typically, X-ray scanners are employed in security checks, enabling inspectors to quickly identify prohibited items in passengers' luggage. However, after prolonged exposure to a large number of X-ray images, inspectors may face challenges in consistently detecting all prohibited items without distraction. Although shift rotations can help mitigate this issue, the associated high labor costs remain problematic.

To address the issue of high labor expenses, a prominent

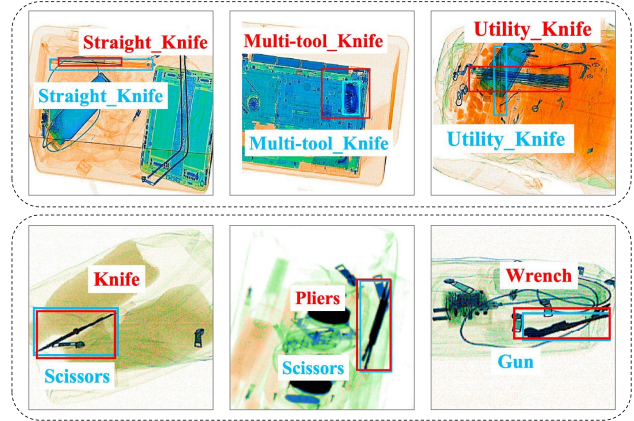


Figure 1. Some detection failures of Group R-CNN [31] caused by imprecise localization (the upper panel) and inaccurate classification (the lower panel). The blue box represents the ground truth and the red box represents the detection results of Group R-CNN.

strategy in X-ray security screening is to incorporate automatic detection technologies to support inspectors. In recent years, automatic X-ray prohibited item detection (PID) has received considerable attention. A number of fully-supervised PID methods [8, 10, 14, 16] have been proposed. These methods usually require large-scale labeled training data with box annotations (involving both bounding boxes and categories of prohibited items in each image). Unfortunately, annotating the bounding box is time-consuming and labor-intensive. Moreover, it imposes high demands on the expertise of annotators [1].

Recently, semi-supervised objection detection methods [4, 9, 11, 30], weakly supervised object detection methods [13, 17, 18, 24], and their combinations [2, 31] have been developed to alleviate the workload of manual annotations. Among these methods, Weakly Semi-Supervised Object Detection with Points (WSSOD-P), which trains the models by a few box annotations and a large number of point annotations, achieves a good balance between annotation cost and detection performance. However, when ap-

plied to X-ray images, existing WSSOD-P methods [2, 31] suffer from two issues: (1) *imprecise localization* caused by weak boundaries, and (2) *inaccurate classification* caused by large intra-class variations and inter-class similarities.

On the one hand, due to the penetration characteristics of X-ray scanners, the boundaries between prohibited items and their surroundings are often weak. Notably, point annotations only provide the approximate locations of prohibited items without the scale information. As a result, the trained model struggles to effectively capture the boundary details, which can make the detection boxes difficult to precisely align with the item boundary, leading to imprecise localization. Some examples are given in the upper panel of Fig. 1. The trained model gives poor localization performance near the boundaries of prohibited items.

On the other hand, each prohibited item category in X-ray images typically exhibits significant intra-class variations and inter-class similarities due to scale changes and different rotations of prohibited items. This variability can easily lead to the inaccurate classification of candidate proposals. Some examples are given in the lower panel of Fig. 1. The trained model tends to misclassify some prohibited items with large scale and rotation changes.

Based on the above analysis, we study the problem of Weakly Semi-Supervised X-ray Prohibited Item Detection with Points (WSSPID-P), aiming at addressing the closely related problems of imprecise localization and inaccurate classification. Imprecise localization causes the positions of candidate boxes to deviate from ground-truth positions, adversely affecting the prediction scores given by the classification branch and leading to inaccurate label predictions. Conversely, inaccurate classification can enforce the model to learn irrelevant features for detecting prohibited items, further resulting in imprecise bounding box positions. Therefore, developing robust feature representations that capture boundary information (to ensure precise localization) and remain insensitive to changes in scale and rotation (to ensure accurate classification) is important.

To this end, we propose a novel Boundary-Category Refinement Network (BCR-Net), which learns boundary-aware features that are robust to scale and rotation variations, for WSSPID-P. Our BCR-Net is built based on Group R-CNN [31] and incorporates two new modules: a Boundary Refinement (BR) module and a Category (CR) module.

Specifically, in the BR module, we develop a dual attention mechanism with a parallel connection to enhance the delineation between prohibited items and background or other items. This module applies reverse and forward attention to multiple levels of feature maps to improve boundary representations. Importantly, the dual attention is adaptively learned in a coarse-to-fine manner. As a result, the BR module not only highlights the salient areas of prohibited items but also progressively captures boundary information,

greatly addressing the problem of imprecise localization.

In the CR module, we integrate contrastive branches into the heads of region proposal network (RPN) and region of interest (ROI), enhancing classification by pulling closer features from the same category and pushing apart features from different categories. In particular, we design a scale- and rotation-aware contrastive loss to reduce variations from the same category and increase the distances between different categories. This is achieved by implicitly imposing scale/rotation perturbations to anchor boxes. Such a way can alleviate the problem of inaccurate classification.

The main contributions of this paper are as follows:

- We propose a novel BCR-Net, which can be effectively trained under a small number of box annotations and a large number of point annotations, for WSSPID-P. BCR-Net facilitates highly effective feature learning under limited supervision, reducing labeling costs while delivering competitive detection performance.
- We develop a BR module to perform dual attention, capturing boundary features and alleviating imprecise localization. Meanwhile, we introduce a CR module to incorporate contrastive learning with a new scale- and rotation-aware contrastive loss, addressing inaccurate classification. The synergy of the two modules enhances boundary awareness and robustness to scale and rotation changes.
- We conduct extensive experiments on four widely-used X-ray datasets to validate the effectiveness of BCR-Net. Notably, it achieves significant performance improvements than state-of-the-art methods under limited annotation settings.

2. Related Work

X-Ray Prohibited Item Detection Existing X-ray prohibited item detection methods focus on addressing the detection difficulty caused by ubiquitous item overlapping and occlusion in X-ray images. Wei *et al.* [28] develop a De-Occlusion Attention Module (DOAM), which combines edge attention and region attention for detecting occluded prohibited items. Miao *et al.* [15] propose a Category Balanced Hierarchical Refinement (CHR) method based on a mixed distribution hypothesis. Tao *et al.* [23] introduce a Local Inhibition Module (LIM) that identifies key features while ignoring irrelevant occlusion information in X-ray images. Wang *et al.* [26] present a Selective Dense Attention Network (SDANet) to enhance detection performance based on dense attention and dependency refinement modules. Isaac-Medina *et al.* [5] reveal the high correlation between false negatives and the size of prohibited items, observing that single-stage anchor-free detectors perform poorly when detecting heavily occluded items.

The above methods typically rely on a large amount of bounding box annotations for training, leading to high annotation costs. Different from these methods, our method

studies WSSPID-P, which involves a large number of point annotations and only a small number of bounding box annotations for model training. Such a manner effectively reduces annotation costs.

Semi-Supervised/Weakly-Supervised Object Detection

Zhou *et al.* [32] develop instant-teaching, which enhances the detection performance based on instant pseudo-labels and extended weak-strong data augmentation. Shehzadi *et al.* [21] introduce sparse semi-DETR, which addresses the issues of inaccurate pseudo-labels and prediction overlaps within the DETR framework by incorporating query optimization and pseudo-label filtering modules. Bilen *et al.* [1] introduce the Weakly Supervised Deep Detection Network (WSDDN) by integrating Multiple Instance Learning (MIL) into weakly supervised object detection. Tang *et al.* [22] design Proposal Clustering Learning (PCL) to expand detection areas by proposal clustering. Chen *et al.* [3] propose P2BNet, which generates high-quality proposal bags to bridge the performance gap between point supervision detectors and bounding box supervision detectors. PointOBB [12] learns object angles and scales by collaboration between multiple views.

Existing point-supervised methods require point annotations to be centered on the object, rendering the annotation process complicated. In contrast, WSSPID-P only requires point annotations to be labeled at any position on the object.

Weakly Semi-Supervised Object Detection with Points

(WSSOD-P) Chen *et al.* [2] develop point DETR, which incorporates a point encoder that encodes the positions and classes of points into object queries and predicts bounding boxes using a single-stage feature map. Zhang *et al.* [31] introduce Group R-CNN to generate proposals based on instance-level proposal grouping and allocation strategies. They address model convergence difficulties with instance-aware representation learning.

Although the above methods have shown promising results on natural images, they often suffer from the problems of inaccurate classification and imprecise localization when applied to WSSPID-P because of significant differences between X-ray and natural images. In this paper, we develop a novel BCR-Net to address these two close-related problems considering the characteristics of X-ray images.

3. Method

3.1. Overview

In this paper, we propose a Boundary-Category Refinement Network (BCR-Net) for WSSPID-P. The overview of BCR-Net is given in Fig. 2. Building upon Group R-CNN [31], BCR-Net introduces two key modules: a Boundary Refinement (BR) module and a Category Refinement (CR) module. Following Group R-CNN, the training process of BCR-Net is comprised of three stages. First, the model is pre-

trained to generate bounding boxes from point annotations by using a small number of samples with bounding box annotations. Then, the pretrained model predicts pseudo-bounding box annotations for samples with only point annotations. Finally, the model is fine-tuned as a prohibited item detector by using both the bounding box annotations and the generated pseudo-bounding box annotations.

Specifically, we first feed a batch of X-ray images into Group R-CNN (which consists of a backbone network, a Feature Pyramid Network (FPN), and several RoI heads). Then, the BR module, which applies reverse and forward attention to multiple levels of feature maps, captures the salient areas of prohibited items while emphasizing the boundaries at different levels. Technically, for each level of the feature map, we apply the dual-attention mechanism to generate a dual-attention feature map considering the feature map obtained at the higher level. Thus, the coarse-to-fine dual-attention feature maps can be obtained. In this process, the reverse attention can help maintain the model’s sensitivity to boundary details and the forward attention helps the model retain critical information for the primary areas of prohibited items. The dual-attention mechanism effectively reduces localization errors due to weak boundaries, enabling pseudo-bounding boxes to align more precisely with prohibited item boundaries.

Based on the dual-attention feature maps generated by the BR module, the CR module, which pulls closer features from the same category while pushing apart features from different categories, enhances classification based on contrastive learning. Technically, the CR module introduces contrastive branches to RPN and RoI heads, incorporating a scale- and rotation-aware contrastive loss. This design allows the model to handle variations in scale and rotation, effectively reducing the influence of intra-class and inter-class variability on classification accuracy. Such a manner enables the model to achieve better intra-class consistency and inter-class separability in the feature space, leading to improved classification performance.

By addressing the closely related problems of *imprecise localization* and *inaccurate classification*, the BR and CR modules enable the model to achieve enhanced localization and classification performance for WSSPID-P.

3.2. Boundary Refinement (BR) Module

For WSSPID-P, the majority of annotations are point annotations, and the number of box annotations that indicate the scale of prohibited items is very limited. Consequently, existing methods cannot accurately identify the weak boundaries of the prohibited items. To address this issue, we develop the BR module, which introduces a dual attention mechanism based on reverse and forward attention. By performing dual attention at different levels of FPN, the model can capture salient areas of prohibited items while empha-

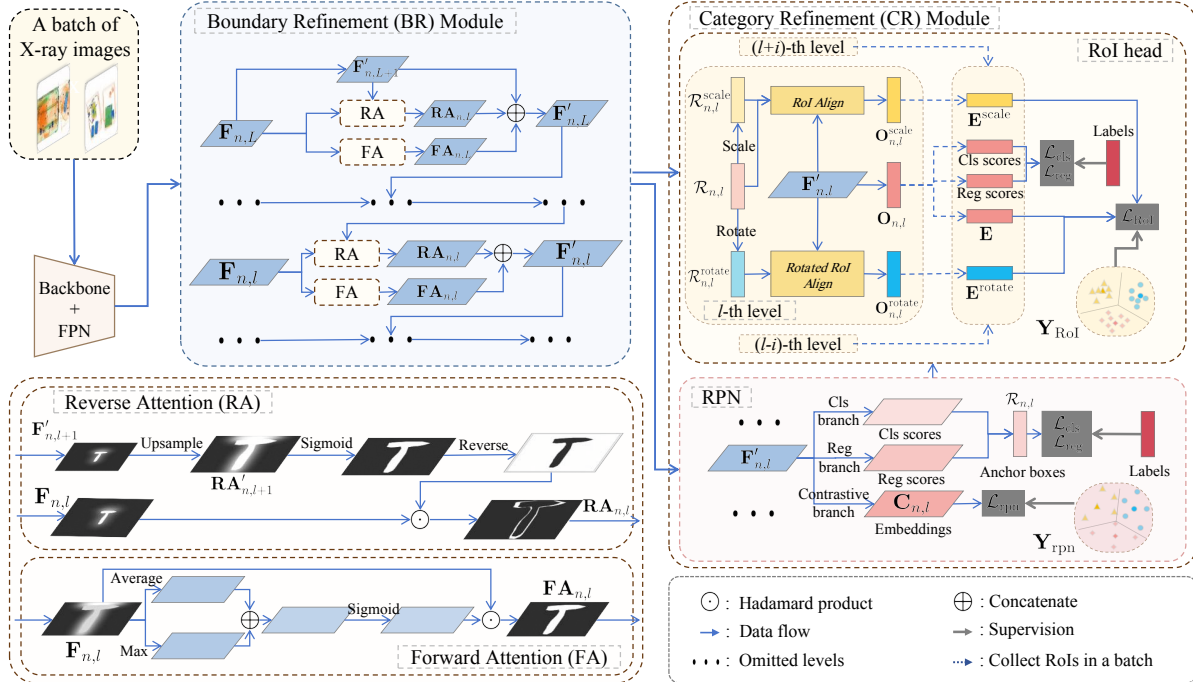


Figure 2. Overview of our proposed BCR-Net, which consists of a BR module and a CR module. The BR module constructs a dual attention mechanism (reverse and forward attention) and progressively captures boundary information. The CR module incorporates contrastive learning into the RPN and ROI heads with a scale- and rotation-aware contrastive loss.

sizing weak boundaries at multiple levels.

Generally, our reverse attention is computed from the high-layer to the low-layer in a coarse-to-fine manner. By progressively capturing salient areas and boundary information, we can achieve more accurate object boundary localization. The core idea behind this is to fuse the reverse attention map generated from high-level feature maps with the low-level feature map, effectively extracting boundary features at different levels. Note that reverse attention focuses more on the boundaries of prohibited items. Hence, it adversely ignores the salient areas of prohibited items. Therefore, we also generate forward attention to emphasize the salient areas, preventing reverse attention from dominating the entire detection process.

Specifically, given an X-ray image I_n (n denotes the n -th image in the training set), we feed it into the backbone and FPN to obtain multi-level feature maps $\{\mathbf{F}_{n,l}\}_{l=1}^L$. Here, $\mathbf{F}_{n,l} \in \mathbb{R}^{H_l \times W_l \times C_l}$ denotes the feature map at the l -th layer; L is the total number of feature map levels in FPN; H_l , W_l , and C_l represent the height, width, and number of channels of $\mathbf{F}_{n,l}$, respectively.

Initially, we apply a convolution layer to $\mathbf{F}_{n,L}$, generating the initial reverse attention feature map $\mathbf{F}'_{n,L+1} = \mathbf{RA}'_{n,L+1}$. This initial reverse attention serves as the initial input for the subsequent reverse attention operation. Note that $\mathbf{RA}'_{n,L+1}$ is only used as an initial feature map for the

BR module and does not participate in the subsequent detection process.

We perform reverse attention from the highest layer ($l = L$) to the lowest layer ($l = 1$). For each level l , we first adjust the size of the reverse attention feature map $\mathbf{F}'_{n,l+1}$ from the $(l+1)$ -th level to match the size of the feature map at the l -th layer. To achieve this, we use bilinear interpolation to generate a temporary feature map $\mathbf{RA}'_{n,l+1}$, ensuring that its dimensions are consistent with $\mathbf{RA}_{n,l}$. That is,

$$\mathbf{RA}'_{n,l+1} = \Gamma(\mathbf{F}'_{n,l+1}), \quad (1)$$

where $\Gamma(\cdot)$ denotes the bilinear interpolation operation.

Next, we use the Sigmoid function to generate reverse attention weights and apply them to the current layer feature map $\mathbf{F}_{n,l}$ with the multiplication operation, followed by a convolutional layer, obtaining the reverse attention map $\mathbf{RA}_{n,l}$. The above process can be expressed as

$$\mathbf{RA}_{n,l} = \text{Conv}((1 - \sigma(\mathbf{RA}'_{n,l+1})) \odot \mathbf{F}_{n,l}), \quad (2)$$

where σ represents the Sigmoid function and \odot indicates element-wise multiplication. The purpose of the above operation is to modulate the current layer feature map based on the weights generated by the Sigmoid function, thereby highlighting boundary features (as illustrated in Fig. 2).

Meanwhile, we apply forward attention to guide the model, ensuring that the model also focuses on the salient

areas (as illustrated in Fig. 2). Technically, for $\mathbf{F}_{n,l}$, we use spatial attention to generate forward attention as

$$\mathbf{FA}_{n,l} = \mathbf{F}_{n,l} \odot \sigma \left(\text{Conv} \left(\overline{\mathbf{F}}_{n,l} \oplus \max_c(\mathbf{F}_{n,l}^c) \right) \right), \quad (3)$$

where $\overline{\mathbf{F}}_{n,l}$ represents the averaging operation across all channels of $\mathbf{F}_{n,l}$; \oplus represents the concatenation operation; $\mathbf{F}_{n,l}^c$ denotes the c -th channel feature of $\mathbf{F}_{n,l}$; $\mathbf{FA}_{n,l}$ denotes the forward attention map.

After obtaining forward attention, we perform a weighted sum of the reverse attention map $\mathbf{RA}_{n,l}$, the forward attention map $\mathbf{FA}_{n,l}$, and the temporary feature map $\mathbf{RA}'_{n,l+1}$ to obtain the dual attention map $\mathbf{F}'_{n,l}$ at the current layer:

$$\mathbf{F}'_{n,l} = \lambda_l^1 \mathbf{RA}_{n,l} + \lambda_l^2 \mathbf{FA}_{n,l} + \lambda_l^3 \mathbf{RA}'_{n,l+1}, \quad (4)$$

where λ_l^1 , λ_l^2 , and λ_l^3 are learnable parameters at the l -th level.

Finally, we utilize the dual attention maps $\{\mathbf{F}'_{n,l}\}_{l=1}^L$ for subsequent detection.

3.3. Category Refinement (CR) Module

As we mentioned above, the prohibited items may exhibit significantly different shapes, sizes, and orientations, leading to large intra-class variations and inter-class similarities. This makes the model challenging to classify prohibited items in images. To address this, we propose the CR module by introducing contrastive learning to both RPN and RoI heads. Thus, we can enhance the classification performance by pulling closer features from the same category and pushing apart features from the different categories. In the RoI head, we design a scale- and rotation-aware contrastive loss to improve the model's robustness against intra-class variations and inter-class similarities.

Contrastive Branch in the RPN head Technically, in RPN, we add a contrastive branch in parallel to the classification and regression branches. The classification and regression branches are responsible for extracting information related to category discrimination and object localization, respectively. Meanwhile, in the contrastive branch, $\mathbf{F}'_{n,l}$ is fed into several convolutional layers to extract the feature embeddings $\mathbf{C}_{n,l} \in \mathbb{R}^{H_l \times W_l \times (D \times N_{\text{base}})}$, where D denotes the dimension of the features embedding and N_{base} represents the number of anchors.

After passing through RPN and the contrastive branch, high-scoring anchors $\mathcal{R}_{n,l}$ are retained and forwarded to the RoI head for further refinement. Here, $\mathcal{R}_{n,l} = \{\mathbf{R}_{n,l}^m\}_{m=1}^{M_l}$; $\mathbf{R}_{n,l}^m$ denotes the m -th high-scoring anchor box (consisting of top-left and bottom-right corners); M_l indicates the number of high-scoring anchors at level l .

Scale and Rotation Transformations To reduce the model's sensitivity to intra-class and inter-class variations,

we perform scale and rotation transformations on $\mathcal{R}_{n,l}$ before feeding them to the RoI head.

For the scale transformation, we add perturbations to each anchor box in $\mathcal{R}_{n,l}^m$ according to a scaling factor $\Delta = (\delta_x^m, \delta_y^m)$. Hence, the scaled bounding box $\mathbf{R}_{n,l}^{m,\text{scale}}$ is represented as

$$\mathbf{R}_{n,l}^{m,\text{scale}} = \left(cx_{n,l}^m - \frac{\delta_x^m w_{n,l}^m}{2}, cy_{n,l}^m - \frac{\delta_y^m h_{n,l}^m}{2}, \right. \\ \left. cx_{n,l}^m + \frac{\delta_x^m w_{n,l}^m}{2}, cy_{n,l}^m + \frac{\delta_y^m h_{n,l}^m}{2} \right), \quad (5)$$

where $cx_{n,l}^m$ and $cy_{n,l}^m$ denote the center coordinates of the anchor box; $w_{n,l}^m$ and $h_{n,l}^m$ denote the weight and height of the anchor box, respectively; δ_x^m and δ_y^m are randomly sampled from $U(0.9, 1.1)$; $U(\cdot)$ denotes the uniform distribution.

For the rotation transformation, we employ a principal component analysis (PCA) to determine the main direction of the prohibited item within the anchor box. Technically, we first segment the feature map $\mathbf{F}'_{n,l}$ according to anchor boxes $\mathcal{R}_{n,l}$, obtaining $\{\mathbf{P}_{n,l}^m\}_{m=1}^{M_l}$. Here $\mathbf{P}_{n,l}^m \in \mathbb{R}^{H_m \times W_m \times C_l}$ denotes the feature map corresponding to the m -th anchor box. Then, we compress the channels to one dimension, resulting in $\{\mathbf{P}'_{n,l}^m\}_{m=1}^{M_l}$, where $\mathbf{P}'_{n,l}^m \in \mathbb{R}^{H_m \times W_m}$. Next, we calculate the mean $\mu_{n,l}^m$ and covariance matrix $\mathbf{A}_{n,l}^m$ for each feature map, that is,

$$\mu_{n,l}^m = \frac{1}{H_m W_m} \sum_{i=1}^{H_m} \sum_{j=1}^{W_m} \mathbf{P}'_{n,l}^m[i, j], \\ \mathbf{A}_{n,l}^m = \frac{1}{H_m W_m - 1} \sum_{i=1}^{H_m} \sum_{j=1}^{W_m} \left(\mathbf{P}'_{n,l}^m[i, j] - \mu_{n,l}^m \right)^2. \quad (6)$$

Subsequently, we compute the eigenvalues and eigenvectors of the covariance matrix $\mathbf{A}_{n,l}^m$. We define the eigenvector corresponding to the largest eigenvalue as $\mathbf{v}_{n,l}^m = (v_{n,l}^{x,m}, v_{n,l}^{y,m})$. The principal orientation of the prohibited item is then given by $\theta_{n,l}^m = -\tan^{-1} \left(v_{n,l}^{x,m} / v_{n,l}^{y,m} \right)$. After the rotation transformation, the bounding box is represented as $\mathbf{R}_{n,l}^{m,\text{rotate}} = (cx_{n,l}^m - w_{n,l}^m/2, cy_{n,l}^m - h_{n,l}^m/2, cx_{n,l}^m + w_{n,l}^m/2, cy_{n,l}^m + h_{n,l}^m/2, \theta_{n,l}^m)$. Based on the above, given $\mathcal{R}_{n,l}$, we obtain $\mathcal{R}_{n,l}^{\text{scale}}$ and $\mathcal{R}_{n,l}^{\text{rotate}}$.

Contrastive Branch in the RoI Head For $\mathcal{R}_{n,l}$ and $\mathcal{R}_{n,l}^{\text{scale}}$, we use RoI align to extract RoIs from $\mathbf{F}'_{n,l}$, obtaining $\mathbf{O}_{n,l}$ and $\mathbf{O}_{n,l}^{\text{scale}}$, respectively. For $\mathcal{R}_{n,l}^{\text{rotate}}$, we employ rotated RoI align to extract RoIs, obtaining $\mathbf{O}_{n,l}^{\text{rotate}}$. We send $\mathbf{O}_{n,l}$ into the classification and regression branches of the RoI head. Concurrently, we design a contrastive branch in the RoI head, where we feed $\mathbf{O}_{n,l}$, $\mathbf{O}_{n,l}^{\text{scale}}$, and $\mathbf{O}_{n,l}^{\text{rotate}}$ into the contrastive branch for obtaining feature embeddings.

Given a batch of images, we can obtain the feature embeddings of the three types of RoIs, denoted as \mathbf{E} , $\mathbf{E}^{\text{scale}}$, and $\mathbf{E}^{\text{rotate}} \in \mathbb{R}^{BM \times D}$, where B represents the batch size, M is the total number of high-scoring anchor boxes across all levels, and D is the dimension of the feature embedding.

Scale- and Rotation-Aware Contrastive Loss We propose a scale- and rotation-aware contrastive loss to enhance class discriminability based on the similarity between the feature embeddings and class prototypes. Specifically, we compute the similarities between each feature embedding and class prototypes as well as the similarities between different feature embeddings from different categories.

We denote the class prototypes for the contrastive branch in the RoI head as $\mathbf{Y}_{\text{RoI}} \in \mathbb{R}^{(N_{\text{cls}}+1) \times D}$, where $N_{\text{cls}} + 1$ denotes the number of prohibited item categories and the background class. Then, we compute the similarity matrix between these three types of feature embeddings and their corresponding prototypes (denoted as $\mathbf{S}_{\text{fp}}^{(t)}$) as well as that between feature embeddings (denoted as $\mathbf{S}_{\text{ff}}^{(t)}$)

$$\mathbf{S}_{\text{fp}}^{(t)} = \frac{\mathbf{E}^{(t)} \mathbf{Y}_{\text{RoI}}^{\text{T}}}{\tau}, \quad \mathbf{S}_{\text{ff}}^{(t)} = \frac{\mathbf{E}^{(t)} (\mathbf{E}^{(t)})^{\text{T}}}{\tau}, \quad (7)$$

where $t = \{0, 1, 2\}$ denotes the standard feature embedding \mathbf{E} , scale-adjusted feature embedding $\mathbf{E}^{\text{scale}}$, and rotation-adjusted feature embedding $\mathbf{E}^{\text{rotate}}$, respectively; τ denotes the temperature parameter typically set to 0.2.

To avoid computing the contrastive loss of feature embeddings with themselves, we define a mask matrix $\mathbf{M}^{\text{ff}} \in \mathbb{R}^{R \times R}$, with diagonal elements set to zero and all off-diagonal elements set to one. We also introduce a label mask $\mathbf{M}^{\text{label}} \in \mathbb{R}^{R \times R}$ to identify pairs of feature embeddings with the same label. We define a positive sample mask $\mathbf{M}^{\text{pos}} \in \mathbb{R}^{R \times R}$ to denote positive sample pairs.

For the contrastive loss of the i -th feature embedding, we compute its logarithmic probability relative to other feature embeddings and class prototypes. The logarithmic probability of a sample is defined as

$$\log p_i^{(t)} = \mathbf{S}_{\text{fp},i}^{(t)} - \log \left(\sum_{j=1}^R e^{\mathbf{S}_{\text{ff},ij}^{(t)}} \cdot \mathbf{M}_{ij}^{\text{ff}} + \sum_{d=1}^{N_{\text{cls}}+1} e^{\mathbf{S}_{\text{fp},id}^{(t)}} + \epsilon \right), \quad (8)$$

where i and j denote the embeddings for the i -th and the j -th images, d denotes the d -th class, and $\epsilon = 10^{-10}$ is a small constant to prevent numerical instability.

Based on the aforementioned similarities and the masking mechanism, we define the loss as

$$\mathcal{L}_{\text{RoI}} = -\frac{1}{R} \sum_{t=0}^2 \sum_{i=1}^R \frac{\sum_{j=1}^R \left(\log p_{i,j}^{(t)} \cdot \mathbf{M}_{ij}^{\text{ff}} \cdot \mathbf{M}_{ij}^{\text{label}} \cdot \mathbf{M}_{ij}^{\text{pos}} \right)}{\sum_{j=1}^R \left(\mathbf{M}_{ij}^{\text{label}} \cdot \mathbf{M}_{ij}^{\text{ff}} \cdot \mathbf{M}_{ij}^{\text{pos}} \right)}, \quad (9)$$

Similarly, for the feature embeddings $\mathbf{C}_{n,l}$ in the RPN, we apply a similar way to compute the loss, denoted as \mathcal{L}_{rpn} .

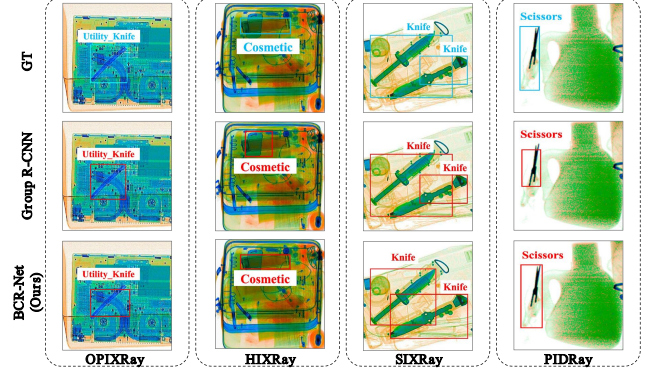


Figure 3. Performance comparison between our BCR-Net and Group R-CNN.

Hence, the total contrastive loss function is then defined as

$$\mathcal{L}_{\text{contrast}} = \mathcal{L}_{\text{RoI}} + \mathcal{L}_{\text{rpn}}. \quad (10)$$

4. Experiments

4.1. Experimental Settings

Datasets We evaluate our BCR-Net on four commonly used X-ray datasets, including OPIXray[28], HIXray[23], SIXray[15], and PIDray[26]. The OPIXray dataset contains 5 categories with a total of 8,885 images. The SIXray dataset comprises 6 categories with a total of 1,059,231 images. We use 8,929 images that contain prohibited items for training and testing. The HIXray dataset consists of 8 categories with 45,364 images. The PIDray dataset includes 12 categories with a total of 124,486 images. We select 47,677 images containing prohibited items for training and testing. We randomly select 5% of the images with box annotations and the remaining 95% of the images with point annotations for training. We randomly generate point annotations within the bounding box as done in Group R-CNN [31].

Implementation Details Our BCR-Net is implemented based on Group R-CNN and employ ResNet-50 as the backbone. We train the model using stochastic gradient descent (SGD) on 2 NVIDIA RTX 3090 GPUs, with an initial learning rate of 0.01. Due to the limited availability of box annotations, we set the total number of training epochs to 48 and the batch size to 2 to ensure convergence of the model. In the contrastive branch, we set the dimension of the feature embeddings to 256. All the other settings remain consistent with those of Group R-CNN. We report average precision (AP) and AP₅₀ as the evaluation metrics. Our source code is temporarily attached in the Supplement.

4.2. Comparison with State-of-the-Art Methods

We perform a comprehensive comparison between BCR-Net and various box-supervised detectors. In addition,

Table 1. Performance comparison results (%) between our method and state-of-the-art methods on four X-ray datasets.

Method	Backbone	OPIXray		HIXray		SIXray		PIDray	
		AP	AP ₅₀	AP	AP ₅₀	AP	AP ₅₀	AP	AP ₅₀
Box-supervised detectors									
Faster R-CNN [19]	ResNet-50	40.06	89.87	45.06	84.42	56.31	89.65	64.73	82.37
RetinaNet [7]	ResNet-50	40.53	90.02	46.88	83.85	51.17	84.88	66.78	80.95
YOLOv8-s [6]	CSPDarkNet	37.90	83.40	43.60	77.00	55.70	84.20	66.00	77.50
FCOS [25]	ResNet-50	38.36	89.60	45.80	86.80	53.80	86.80	67.00	83.10
Deformable DETR [33]	ResNet-50	37.70	88.90	49.80	82.05	56.10	89.20	70.12	82.97
Image-supervised detectors									
PCL [22]	ResNet-50	-	2.87	-	4.21	-	1.48	-	7.76
WSOD2 [29]	ResNet-50	-	3.11	-	5.18	-	1.65	-	9.22
OD-WSCL [20]	ResNet-50	-	4.21	-	6.87	-	1.87	-	9.17
Point-supervised detectors									
P2BNet [3]	ResNet-34	1.04	5.22	6.61	18.41	2.11	8.21	6.51	15.83
P2BNet [3]	ResNet-50	3.32	15.50	10.87	25.23	3.43	10.57	8.98	19.77
I ² OL-Net [27]	ResNet-34	10.72	38.12	29.70	74.50	22.45	61.84	29.91	51.88
I ² OL-Net [27]	ResNet-50	15.09	50.62	30.62	75.73	26.24	67.53	31.82	55.43
WSSPID-P detectors									
Group R-CNN [31]	ResNet-50	28.30	76.65	44.80	75.31	25.32	61.39	54.62	74.83
BCR-Net (ours)	ResNet-50	29.04	79.21	47.01	78.42	31.82	69.73	57.92	79.04

we compare image-supervised object detectors, point-supervised object detectors, and WSSPID-P detectors. The results are shown in Table 1. Fig. 3 gives some detection results obtained by our BCR-Net and Group R-CNN on four X-ray datasets.

From Table 1, it is evident that all box-supervised detectors show promising performance across the datasets. This can be attributed to the fact that box annotations provide accurate location information for prohibited items, enabling the model to learn rich localization information and the detailed features required for classification. In contrast, the three image-supervised detectors achieve the lowest accuracy among all detectors. Note that the AP of some image-supervised detectors is nearly zero (we denote these results as ‘-’). The poor performance of these detectors arises from the difficulty of image-supervised detectors in distinguishing between background and prohibited items caused by the problems of imprecise localization and inaccurate classification. In some complex X-ray images, although accurate proposals can be generated through selective search, they may be discarded during the subsequent MIL process due to significant overlapping and occlusion.

The detection performance of point-supervised detectors lies between that of box-supervised and image-supervised detectors across four datasets. Although point-supervised methods offer lower annotation costs, they fail to provide any localization information related to prohibited items, making it difficult for the model to learn the scale and shape of these items. Furthermore, point supervision requires an-

Table 2. Ablation study results (%) on the influence of BR module and CR module.

BR	CR	SIXray		PIDray	
		AP	AP ₅₀	AP	AP ₅₀
×	×	25.32	61.39	54.62	74.83
✓	×	29.81	67.09	56.22	76.73
×	✓	27.92	63.54	57.12	77.14
✓	✓	31.82	69.73	57.92	79.04

notators to annotate points near the centers of prohibited items, increasing the workload. In contrast, WSSPID-P detectors only require a random point to be annotated within the area of the prohibited item.

BCR-Net performs effective feature learning under limited annotations by combining box annotations and point annotations. By effectively combining the CR module and the BR module, BCR-Net demonstrates a significant enhancement in both localization and classification capabilities compared with the baseline. The above experiments show the effectiveness of our method.

4.3. Ablation Studies

Influence of the BR Module and the CR Module Table 2 presents the ablation study results on the BR module and the CR module. We can see that BCR-Net can achieve better performance when the CR module or the BR module is used. Meanwhile, BCR-Net demonstrates a signifi-

Table 3. Ablation study results (%) on the influence of the dual-attention in the CR module.

FA	RA	SIXray		PIDray	
		AP	AP ₅₀	AP	AP ₅₀
×	×	25.32	61.39	54.62	74.83
✓	×	27.44	64.83	54.35	75.25
×	✓	29.32	66.75	55.94	76.36
✓	✓	29.81	67.09	56.22	76.73

Table 4. Ablation study results (%) on the influence of the contrastive branch in the RPN and RoI heads.

RPN	RoI head	SIXray		PIDray	
		AP	AP ₅₀	AP	AP ₅₀
×	×	25.32	61.39	54.62	74.83
✓	×	26.02	62.47	55.82	76.15
×	✓	27.43	63.16	56.87	76.90
✓	✓	27.92	63.54	57.12	77.14

cant improvement in AP and AP_{50} over the baseline across all datasets when both the CR and BR modules are jointly used. The BR module performs dual attention to enhance boundary information while the CR module performs scale- and rotation-aware contrastive learning to improve the intra-class compactness and inter-class separability. The joint learning of the two modules not only ensures class distinction but also enhances boundary information, effectively addressing the problems of imprecise localization and inaccurate classification in X-ray images.

Influence of the Dual Attention In the CR module, we perform dual attention (including Forward Attention (FA) and Reverse Attention (RA)). Table 3 presents the ablation study results on FA and RA. As shown in Table 3, when only FA is used in the CR module, the model demonstrates improvements in terms of AP_{50} across all datasets. When RA is added to the CR module, the model achieves better performance across all datasets, with notable improvements in AP_{50} . This indicates that RA effectively facilitates the model in capturing boundary information of prohibited items, leading to higher precision in localization. When both FA and RA are used simultaneously, the model achieves its optimal performance. This suggests that a complementary relationship exists between FA and RA: RA compensates for the shortcomings of FA in capturing object boundaries, while FA ensures that RA is not dominated by boundaries during the subsequent detection process. By combining FA and RA, the model can focus on both the salient areas and boundaries of prohibited items.

Influence of the Contrastive Branch in RPN and RoI Heads Table 4 gives the ablation study results on the contrastive branches in the RPN and RoI heads of the CR mod-

Table 5. Ablation study results (%) on the influence of the scale- and rotation-aware contrastive loss in the CR module.

scale loss	rotate loss	SIXray		PIDray	
		AP	AP ₅₀	AP	AP ₅₀
×	×	25.32	61.39	54.62	74.83
✓	×	26.73	62.44	55.40	75.45
×	✓	27.02	62.90	56.19	76.46
✓	✓	27.43	63.16	56.87	76.90

ule. When the contrastive branch is introduced into RPN, the model is enforced to learn the features of different anchors when selecting proposals, facilitating in generation of high-quality proposals. When the contrastive branch is incorporated into the RoI head, the model shows performance improvements across all datasets. The performance improvements obtained by BCR-Net with the contrastive branches in the ROI head are more evident than those with the contrastive branch in RPN. The RPN is in the initial stage of proposal generation while the RoI head is positioned at a deeper stage of feature learning. By introducing the contrastive branch into the RoI head, the high-level contextual information can be exploited for better performance. When the contrastive branch is simultaneously integrated into both the RPN and RoI heads, the model achieves the best performance.

Influence of the Scale- and Rotation-Aware Contrastive Loss Table 5 gives the ablation study results for the scale- and rotation-aware contrastive loss. Our method with only the rotation-aware contrastive loss achieves better performance than that with only the scale-aware contrastive loss. This can be attributed to the nature of prohibited items in X-ray images, where complex rotational variations with diverse orientations exist. This requires a great demand on the capacity of the model to generalize across different viewpoints. The rotation-aware contrastive loss assists the model in effectively learning object orientation changes, thereby enhancing detection performance under complex conditions. Our method achieves the best performance when both scale-aware and rotation-aware contrastive losses are jointly used, demonstrating the effectiveness of the proposed contrastive loss.

5. Conclusion

In this paper, we propose a novel BCR-Net for WSSPID-P. BCR-Net achieves effective feature learning under a mixture of a small number of box annotations and a large number of point annotations. BCR-Net introduces a BR module and a CR module to perform dual attention and scale- and rotation-aware contrastive learning, respectively. Such a way effectively addresses the problems of imprecise localization and inaccurate classification. Experiments on pub-

lic X-ray datasets show that BCR-Net achieves much better performance than state-of-the-art WSSPID-P detectors.

References

- [1] Hakan Bilen and Andrea Vedaldi. Weakly supervised deep detection networks. In *Proceedings of the IEEE/CVF Conference on Computer Vision and Pattern Recognition*, pages 2846–2854, 2016. 1, 3
- [2] Liangyu Chen, Tong Yang, Xiangyu Zhang, Wei Zhang, and Jian Sun. Points as queries: Weakly semi-supervised object detection by points. In *Proceedings of the IEEE/CVF Conference on Computer Vision and Pattern Recognition*, pages 8823–8832, 2021. 1, 2, 3
- [3] Pengfei Chen, Xuehui Yu, Xumeng Han, Najmul Hassan, Kai Wang, Jiachen Li, Jian Zhao, Humphrey Shi, Zhenjun Han, and Qixiang Ye. Point-to-box network for accurate object detection via single point supervision. In *Proceedings of the European Conference on Computer Vision*, pages 51–67, 2022. 3, 7
- [4] Wei Hua, Dingkan Liang, Jingyu Li, Xiaolong Liu, Zhikang Zou, Xiaoqing Ye, and Xiang Bai. Sood: Towards semi-supervised oriented object detection. In *Proceedings of the IEEE/CVF Conference on Computer Vision and Pattern Recognition*, pages 15558–15567, 2023. 1
- [5] Brian KS Isaac-Medina, Seyma Yucer, Neelanjan Bhowmik, and Toby P Breckon. Seeing through the data: A statistical evaluation of prohibited item detection benchmark datasets for x-ray security screening. In *Proceedings of the IEEE/CVF Conference on Computer Vision and Pattern Recognition*, pages 524–533, 2023. 2
- [6] Glenn Jocher, Ayush Chaurasia, and Jing Qiu. Ultralytics YOLO, 2023. 7
- [7] Tsung-Yi Lin, Priya Goyal, Ross Girshick, Kaiming He, and Piotr Dollár. Focal loss for dense object detection. In *Proceedings of the IEEE/CVF International Conference on Computer Vision*, pages 2980–2988, 2017. 7
- [8] Aishan Liu, Jun Guo, Jiakai Wang, Siyuan Liang, Renshuai Tao, Wenbo Zhou, Cong Liu, Xianglong Liu, and Dacheng Tao. {X-Adv}: Physical adversarial object attacks against x-ray prohibited item detection. In *32nd USENIX Security Symposium (USENIX Security 23)*, pages 3781–3798, 2023. 1
- [9] Chang Liu, Weiming Zhang, Xiangru Lin, Wei Zhang, Xiao Tan, Junyu Han, Xiaomao Li, Errui Ding, and Jingdong Wang. Ambiguity-resistant semi-supervised learning for dense object detection. In *Proceedings of the IEEE/CVF Conference on Computer Vision and Pattern Recognition*, pages 15579–15588, 2023. 1
- [10] Dongming Liu, Jianchang Liu, Peixin Yuan, Feng Yu, et al. A lightweight dangerous liquid detection method based on depthwise separable convolution for X-ray security inspection. *Computational Intelligence and Neuroscience*, 2022, 2022. 1
- [11] Liang Liu, Boshen Zhang, Jiangning Zhang, Wuhao Zhang, Zhenye Gan, Guanzhong Tian, Wenbing Zhu, Yabiao Wang, and Chengjie Wang. Mixteacher: Mining promising labels with mixed scale teacher for semi-supervised object detection. pages 7370–7379, 2023. 1
- [12] Junwei Luo, Xue Yang, Yi Yu, Qingyun Li, Junchi Yan, and Yansheng Li. Pointobb: Learning oriented object detection via single point supervision. In *Proceedings of the IEEE/CVF Conference on Computer Vision and Pattern Recognition*, pages 16730–16740, 2024. 3
- [13] Hui Lv, Zhongqi Yue, Qianru Sun, Bin Luo, Zhen Cui, and Hanwang Zhang. Unbiased multiple instance learning for weakly supervised video anomaly detection. In *Proceedings of the IEEE/CVF Conference on Computer Vision and Pattern Recognition*, pages 8022–8031, 2023. 1
- [14] Chunjie Ma, Li Zhuo, Jiafeng Li, Yutong Zhang, and Jing Zhang. EAOD-Net: Effective anomaly object detection networks for X-ray images. *IET Image Processing*, 16(10): 2638–2651, 2022. 1
- [15] Caijing Miao, Lingxi Xie, Fang Wan, Chi Su, Hongye Liu, Jianbin Jiao, and Qixiang Ye. SIXray: A large-scale security inspection X-ray benchmark for prohibited item discovery in overlapping images. In *Proceedings of the IEEE/CVF Conference on Computer Vision and Pattern Recognition*, pages 2119–2128, 2019. 2, 6
- [16] Li Mingyuan, Ma Bowen, Wang Hao, Chen Dongyue, and Jia Tong. Gadget: A geometry-aware X-ray prohibited items detector. *IEEE Sensors Journal*, 24:1665–1678, 2024. 1
- [17] Yongri Piao, Wei Wu, Miao Zhang, Yongyao Jiang, and Huchuan Lu. Noise-sensitive adversarial learning for weakly supervised salient object detection. *IEEE Transactions on Multimedia*, 25:2888–2897, 2022. 1
- [18] Xiaoliang Qian, Yu Huo, Gong Cheng, Chenyang Gao, Xiwen Yao, and Wei Wang. Mining high-quality pseudoinstance soft labels for weakly supervised object detection in remote sensing images. *IEEE Transactions on Geoscience and Remote Sensing*, 61:1–15, 2023. 1
- [19] Shaoqing Ren, Kaiming He, Ross Girshick, and Jian Sun. Faster R-CNN: Towards real-time object detection with region proposal networks. *Advances in Neural Information Processing Systems*, 28, 2015. 7
- [20] Jinhwan Seo, Wonho Bae, Danica J Sutherland, Junhyug Noh, and Daijin Kim. Object discovery via contrastive learning for weakly supervised object detection. In *Proceedings of the European Conference on Computer Vision*, pages 312–329, 2022. 7
- [21] Tahira Shehzadi, Khurram Azeem Hashmi, Didier Stricker, and Muhammad Zeshan Afzal. Sparse semi-detr: Sparse learnable queries for semi-supervised object detection. In *Proceedings of the IEEE/CVF Conference on Computer Vision and Pattern Recognition*, pages 5840–5850, 2024. 3
- [22] Peng Tang, Xinggang Wang, Song Bai, Wei Shen, Xiang Bai, Wenyu Liu, and Alan Yuille. PCL: Proposal cluster learning for weakly supervised object detection. *IEEE Transactions on Pattern Analysis and Machine Intelligence*, 42(1):176–191, 2018. 3, 7
- [23] Renshuai Tao, Yanlu Wei, Xiangjian Jiang, Hainan Li, Hao-tong Qin, Jiakai Wang, Yuqing Ma, Libo Zhang, and Xianglong Liu. Towards real-world X-ray security inspection:

- A high-quality benchmark and lateral inhibition module for prohibited items detection. In *Proceedings of the IEEE/CVF International Conference on Computer Vision*, pages 10923–10932, 2021. [2](#), [6](#)
- [24] Runzhou Tao, Wencheng Han, Zhongying Qiu, Cheng-Zhong Xu, and Jianbing Shen. Weakly supervised monocular 3d object detection using multi-view projection and direction consistency. In *Proceedings of the IEEE/CVF Conference on Computer Vision and Pattern Recognition*, pages 17482–17492, 2023. [1](#)
- [25] Zhi Tian, Chunhua Shen, Hao Chen, and Tong He. FCOS: Fully convolutional one-stage object detection. In *Proceedings of the IEEE/CVF International Conference on Computer Vision*, pages 9627–9636, 2019. [7](#)
- [26] Boying Wang, Libo Zhang, Longyin Wen, Xianglong Liu, and Yanjun Wu. Towards real-world prohibited item detection: A large-scale X-ray benchmark. In *Proceedings of the IEEE/CVF International Conference on Computer Vision*, pages 5412–5421, 2021. [2](#), [6](#)
- [27] Chenyang Wang, Yan Yan, Jing-Hao Xue, and Hanzi Wang. I²OL-Net: Intra-inter objectness learning network for point-supervised X-ray prohibited item detection. *arXiv preprint arXiv:2405.05920*, 2024. [7](#)
- [28] Yanlu Wei, Renshuai Tao, Zhangjie Wu, Yuqing Ma, Libo Zhang, and Xianglong Liu. Occluded prohibited items detection: An X-ray security inspection benchmark and de-occlusion attention module. In *Proceedings of the ACM International Conference on Multimedia*, pages 138–146, 2020. [2](#), [6](#)
- [29] Zhaoyang Zeng, Bei Liu, Jianlong Fu, Hongyang Chao, and Lei Zhang. WSOD2: Learning bottom-up and top-down objectness distillation for weakly-supervised object detection. In *Proceedings of the IEEE/CVF International Conference on Computer Vision*, pages 8292–8300, 2019. [7](#)
- [30] Jiacheng Zhang, Xiangru Lin, Wei Zhang, Kuo Wang, Xiao Tan, Junyu Han, Errui Ding, Jingdong Wang, and Guanbin Li. Semi-detr: Semi-supervised object detection with detection transformers. In *Proceedings of the IEEE/CVF Conference on Computer Vision and Pattern Recognition*, pages 23809–23818, 2023. [1](#)
- [31] Shilong Zhang, Zhuoran Yu, Liyang Liu, Xinjiang Wang, Aojun Zhou, and Kai Chen. Group r-cnn for weakly semi-supervised object detection with points. In *Proceedings of the IEEE/CVF Conference on Computer Vision and Pattern Recognition*, pages 9417–9426, 2022. [1](#), [2](#), [3](#), [6](#), [7](#)
- [32] Qiang Zhou, Chaohui Yu, Zhibin Wang, Qi Qian, and Hao Li. Instant-teaching: An end-to-end semi-supervised object detection framework. In *Proceedings of the IEEE/CVF conference on computer vision and pattern recognition*, pages 4081–4090, 2021. [3](#)
- [33] Xizhou Zhu, Weijie Su, Lewei Lu, Bin Li, Xiaogang Wang, and Jifeng Dai. Deformable DETR: Deformable transformers for end-to-end object detection. *arXiv preprint arXiv:2010.04159*, 2020. [7](#)

BCR-Net: Boundary-Category Refinement Network for Weakly Semi-Supervised X-Ray Prohibited Item Detection with Points

Supplementary Material

Table 6. Ablation study results (%) on the influence of BR module and CR module.

BR	CR	OPIXray		HIXray	
		AP	AP ₅₀	AP	AP ₅₀
×	×	28.30	76.65	44.80	75.31
✓	×	28.09	76.13	45.06	76.89
×	✓	28.45	77.05	46.53	78.00
✓	✓	28.54	77.24	46.86	78.31

Table 7. Ablation study results (%) on the influence of the dual-attention in the CR module.

FA	RA	OPIXray		HIXray	
		AP	AP ₅₀	AP	AP ₅₀
×	×	28.30	76.65	44.80	75.31
✓	×	28.15	77.33	44.64	77.54
×	✓	28.71	78.43	45.25	78.85
✓	✓	28.85	78.81	45.62	79.17

6. Additional Ablation Studies

Ablation Study Results on the Other Two Datasets Tables 6, 7, 8, and 9 present ablation study results on the OPIXray and HIXray datasets. We can see that the results on these datasets are consistent with those observed on SIXray and PIDray, further validating the effectiveness of the key components (including the BR module, the CR module, the dual attention, the contrastive branch, the scale- and rotation-aware contrastive loss) of our methods in addressing the problems of imprecise localization and inaccurate classification for WSSPID-P.

Notably, as shown in Table 7, when only Forward Attention (FA) is used in the CR module, the model exhibits performance improvements in terms of AP₅₀ across all datasets. Meanwhile, we observe a performance decline in terms of AP on two datasets. Note that FA focuses on the main areas of prohibited items, effectively suppressing background noise. However, such a way causes the model to ignore the boundary information, which is crucial for precise localization, thereby resulting in suboptimal performance. By combining forward attention and backward attention, our method can achieve the best performance across all the datasets.

Influence of Different Box Annotation Ratios of the Training Set Table 10 shows the influence of different box annotation ratios (the ratio between the number of box an-

Table 8. Ablation study results (%) on the influence of the contrastive branch in the RPN and RoI heads.

RPN	RoI head	OPIXray		HIXray	
		AP	AP ₅₀	AP	AP ₅₀
×	×	28.30	76.65	44.80	75.31
✓	×	28.09	76.13	45.06	76.89
×	✓	28.45	77.05	46.53	78.00
✓	✓	28.54	77.24	46.86	78.31

Table 9. Ablation study results (%) on the influence of the scale- and rotation-aware contrastive loss in the CR module.

scale loss	rotate loss	OPIXray		HIXray	
		AP	AP ₅₀	AP	AP ₅₀
×	×	28.30	76.65	44.80	75.31
✓	×	28.35	76.83	45.88	76.99
×	✓	28.38	76.98	46.44	77.92
✓	✓	28.45	77.05	46.53	78.00

Table 10. Ablation study results (%) on the influence of different bounding box ratios.

ratio	OPIXray		HIXray		SIXray		PIDray	
	AP	AP ₅₀	AP	AP ₅₀	AP	AP ₅₀	AP	AP ₅₀
5%	29.04	79.21	47.01	78.42	31.82	69.73	57.92	79.04
10%	29.21	80.12	47.14	80.59	38.21	76.88	58.63	79.50
15%	29.33	80.40	47.20	81.77	41.62	79.49	61.90	79.79
20%	29.35	80.51	47.25	82.02	42.69	80.10	62.03	79.85

notations and the total number of annotations) of the training set on performance. It can be observed that increasing the proportion of box annotations in the training set consistently improves the performance of BCR-Net. This indicates that more box annotations can enable the model to achieve better performance. However, as the box annotation ratio increases, the performance gain becomes not evident. In such cases, the benefit of adding more box annotations becomes limited.